Quantum Thermometry with Single Molecules in Nanoprobes

Esteso, V.; Duquennoy, R.; Ng, R. C.; Colautti, M.; Lombardi, P.; Arregui, G.; Chavez-Angel, E.; Sotomayor-Torres, C. M.; Garcia, P. D.; Hilke, M.

Total number of authors:
11

Published in:
PRX Quantum

Link to article, DOI:
10.1103/PRXQuantum.4.040314

Publication date:
2023

Document Version
Publisher's PDF, also known as Version of record

Featured in Physics

Quantum Thermometry with Single Molecules in Nanoprobes

V. Esteso,[1,2,3,†] R. Duquennoy,[1,4,†] R.C. Ng,[5] M. Colautti,[1,2] P. Lombardi,[1,2] G. Arregui,[5,6] E. Chavez-Angel,[5] C.M. Sotomayor-Torres,[5,7] P.D. Garcia,[8] M. Hilke,[9,10] and C. Toninelli[1,2,*]

[1] *National Institute of Optics [(Consiglio Nazionale delle Ricerche CNR)–INO)], care of European Laboratory for Non-Linear Spectroscopy (LENS), Via Nello Carrara 1, Sesto Fiorentino, 50019, Italy*

[2] *European Laboratory for Non-Linear Spectroscopy (LENS), Via Nello Carrara 1, Sesto Fiorentino 50019, Italy*

[3] *Departamento de Física de la Materia Condensada, Instituto de Ciencia de los Materiales de Sevilla (ICMSE)–Consejo Superior de Investigaciones Científicas (CSIC), Universidad de Sevilla, P. O. Box 1065, Sevilla 41080, Spain*

[4] *Physics Department, University of Naples, Via Cinthia 21, Fuorigrotta 80126, Italy*

[5] *Catalan Institute of Nanoscience and Nanotechnology (ICN2), Consejo Superior de Investigaciones Científicas (CSIC) and Barcelona Institute of Science and Technology (BIST), Universitat Autònoma de Barcelona (UAB) Campus, Bellaterra, Barcelona 08193, Spain*

[6] *Department of Electrical and Photonics Engineering, DTU Electro, Technical University of Denmark, Østeds Plads 343, Kongens Lyngby, DK-2800, Denmark*

[7] *Institución Catalana de Investigación y Estudios Avanzados (ICREA), Passeig Lluis Companys 23, Barcelona 08010, Spain*

[8] *Instituto de Ciencia de Materiales de Madrid (ICMM), Consejo Superior de Investigaciones Científicas (CSIC), Calle Sor Juana Inés de la Cruz 3, Madrid, 28049 Spain*

[9] *Department of Physics, McGill University, Montréal, Quebec H3A 2T8, Canada*

[10] *Department of Physics, University of Florence, Via Sansone 1, Sesto Fiorentino, 50019, Italy*

(Received 22 February 2023; revised 3 July 2023; accepted 2 August 2023; published 20 October 2023)

An understanding of heat transport is relevant to developing efficient strategies for thermal management in areas of study such as microelectronics, as well as for fundamental science purposes. However, the measurement of temperatures in nanostructured environments and in cryogenic conditions remains a challenging task, requiring both high sensitivity and noninvasive approaches. Here, we present a portable nanothermometer based on a molecular two-level quantum system that operates in the (3–20)-K temperature range, with temperatures and spatial resolutions on the order of millikelvins and micrometers, respectively. We validate the performance of this molecular thermometer by estimating the thermal conductivity of a nanopatterned silicon membrane, where we find a quadratic temperature dependence. In addition, we demonstrate two-dimensional temperature mapping via the simultaneous spectroscopy of multiple probes deposited onto such a suspended membrane. Overall, these results demonstrate the unique potential of the proposed molecular thermometer to explore thermal properties with submicron accuracy and unveil related phenomena manifested at cryogenic temperatures.

DOI: 10.1103/PRXQuantum.4.040314

I. INTRODUCTION

The precise measurement of local temperature is crucial for efficient thermal management and control of heat conduction. While this control is a major goal at the macroscale [1–4], it is also extremely relevant at much smaller scales, such as in microelectronics [5–8], biological environments [9,10], and even in fundamental quantum science [11–15]. Despite its technological relevance, efficient thermometry methods are challenging, especially in more complex environments such as those in which cryogenic temperatures or nanoscale dimensions are involved. Under these conditions, thermal conduction is predominantly influenced by factors such as phonon scattering at the sample boundary or interface and phonon confinement, leading to the prediction of

*toninelli@lens.unifi.it

†These authors contributed equally to this work.

non-Fourier heat-conduction regimes [16] including ballistic propagation, Casimir-Knudsen effects [17,18], and phonon hydrodynamics [19]. To explore the underlying physics of such transport regimes, ideal thermal probes should have minimal invasivity, while possessing sufficient sensitivity and spatial resolution to map temperature with nanoscale resolution.

Among the currently available nano- and microthermometric methods [9,10,20], the most prominent ones are those based on thermoelectric effects [21,22] or on optical techniques [23–26], such as the frequency-shift measurement in Raman signals [27,28] or the measurement of the reflectivity change in the case of time- and frequency-resolved thermoreflectance techniques [29,30]. The former approaches enable high sensitivity, reaching down to the millikelvin range. However, they tend to be invasive at the nanoscale and are lacking in their ability to provide information with high spatial or two-dimensional (2D) resolution. Raman-based methods, instead, allow for fast and spatially resolved readout but are inefficient as temperatures decrease below a certain value, depending on the system (typically below 100 K). Moreover, these techniques are only applicable to materials with Raman-active modes. Finally, thermoreflectance techniques require complex on-chip architectures such as the use of a transducer layer interacting with the measured samples [31]. Promising results have been obtained with nanoparticle-based temperature detection, including those relying on luminescence measurements [32–34]. However, such classical approaches are usually optimized for room-temperature operation.

Use of the detection of temperature-induced effects in quantum systems theoretically allows for both low-temperature ranges as well as high sensitivity to be simultaneously reached [35], providing an alternative and promising strategy to measure the temperature of a target and its surroundings. A notable example is that of temperature-induced decoherence in a two-level system (qubit), which leaves the thermal bath largely unperturbed, as no actual thermalization or energy exchange takes place. Furthermore, quantum metrology strategies can be applied to identify optimal measurements, yielding the best precision and accuracy given some interaction Hamiltonian [36, 37]. However, the extreme sensitivity of quantum probes to the environment complicates the decoupling of temperature effects from other sources of decoherence and hinders their deployment within portable solid-state devices.

In this paper, we present a noninvasive nanothermometer based on quantum emitters hosted in molecular crystals and employed as quantum probes. These fluorescent molecules are embedded as interstitial impurities in submicron-sized crystals, which can be positioned on the sample at the microscale and investigated under cryogenic conditions. The precise estimate of the local temperature is obtained from the measurement of the optical-transition line width of the molecules. This new-found thermometer is calibrated by comparing the response of several molecular emitters on different surfaces as a function of the cryostat temperature. By exploiting the absorption of a laser beam impinging on the sample at a controlled power and position, heat conduction in nanostructured silicon membranes is studied as a relevant and representative test bed and characterized with unprecedented sensitivity in the temperature range from 3 to 20 K. Temperature maps are also acquired with discrete sampling of the surface over approximately $40 \times 15\ \mu\text{m}^2$. The investigated area can be readily extended to a few mm^2.

II. CONCEPT AND EXPERIMENTAL SETUP

Polyaromatic hydrocarbon chromophores embedded in appropriate host matrices and cooled down to cryogenic temperatures can be described to first approximation as a two-level system capable of emitting single photons with high brightness, purity, long-term photostability, and indistinguishability [38]. In particular, here we consider dibenzoterrylene (DBT) molecules embedded in anthracene (Ac) nanocrystals (NCx) [39,40] as molecular thermometers. Figure 1 shows the relevant energy levels of DBT-Ac nanocrystals, with S_0 and S_1 being the ground and the excited electronic singlet states, respectively. The zero-phonon line (ZPL) is around 785 nm and its line width is lifetime limited at low temperatures with a full width at half maximum (FWHM), denoted by $\tilde{\gamma}$, such that $\tilde{\gamma} = \Gamma_1/2\pi = 1/(2\pi\tau_1) \simeq 50$ MHz, with τ_1 being the radiative lifetime [39]. In addition to a purely electronic transition, the molecular excited state can decay via internal vibrational states, yielding fluorescence at longer wavelengths. Moreover, electron-phonon coupling with the mechanical excitations of the matrix gives rise to the so-called phonon side bands in the emission spectrum and induces decoherence of the molecular-transition dipole moment as a second-order effect [41–44]. The molecule can thereby also be interpreted as an acute sensor of its local environment, which, at a given temperature, is characterized by a phonon spectral density of states and relative average occupation number, determined the Boltzmann distribution. The exact optomechanical interactions that occur between photons, localized mechanical excitation of the molecules, and phonons is a rich and active area of research [45,46]. Here, we focus more specifically on exploiting the temperature-dependent optical response that results from these interactions. In particular, we will explore the molecular dynamics by considering that the ZPL transition line width (FWHM) is expected to follow a close-to-exponential increase with temperature, according to Ref. [44] (additional details are provided below and in Appendix E).

Toward this goal, excitation spectroscopy is used, whereby the laser frequency ω_L is scanned across the ZPL

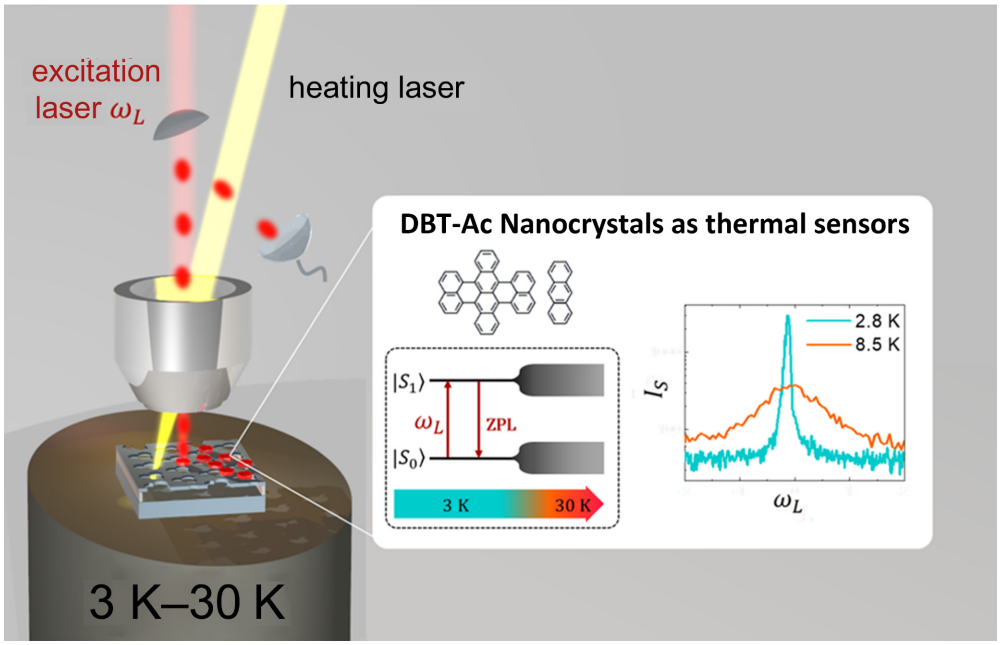

FIG. 1. An illustration of the experimental setup and working principle. A sketch of the experimental setup is shown on the left, in which an excitation laser (red beam) interrogates the molecular thermometers (red disks on a patterned silicon membrane) consisting of dibenzoterrylene (DBT) molecules in anthracene (Ac) nanocrystals (NCx) emitting single photons (red spots), while the heating laser (yellow beam) acts as a controllable heating source. The Stokes-shifted fluorescence intensity (I_S) is collected as a function of ω_L, giving rise to Lorentzian peaks with temperature-dependent line widths. The relevant energy levels (center) of DBT-Ac NCx, where $|S_0\rangle$ and $|S_1\rangle$ represent the singlet ground and excited states, respectively. As the temperature increases, the energy levels, and in consequence the transition lines, broaden in a reproducible way, providing an ideal optical transduction (see the graph on the right).

transition and the red-shifted fluorescence I_S is collected after a long-pass filter. The experiments are done using a confocal microscope in an epifluorescence configuration, as sketched on the left of Fig. 1. More details on the optical setup can be found in Refs. [39,47]. This setup allows for detection with either an electron-multiplied charge-coupled device (EMCCD) camera or single-photon avalanche photodiodes (SPADs). Two SPADs are arranged in the Hanbury Brown–Twiss configuration to detect the single-molecule intensity autocorrelation function (see Fig. 5 in Appendix B).

The characteristic FWHM of the Lorentzian profile obtained from excitation spectroscopy is estimated under different testing conditions. In a first experiment, the temperature of the cryostat (a Montana closed-cycle cryostation) is controlled by local heaters and measured with a thermocouple placed on the cold finger. This setup is used for calibration, as discussed further below (see Sec. III A). In a second series of experiments, we use an extra laser beam (a He:Ne laser) with a central wavelength of $\lambda = 632$ nm focused on the sample as a local heat source (the heating laser in Fig. 1). The wavelength of the heating laser can be arbitrary as long as it does not efficiently excite the two-level transition of our nanoprobe (examples of measurements obtained with another heating laser with 767-nm central wavelength are shown in Figs. 6 and 7 in Appendixes C and D, respectively). We then set up two different configurations, referred to as type I and II from here onward. In the type-I configuration (see Sec. III B), the position of the heating laser can be displaced with respect to a DBT-Ac nanocrystal probe, while single-molecule excitation spectroscopy is performed on said probe. From the line-width broadening, the local temperature on the surface can be estimated as a function of the distance from the heating source. Following this approach, thermal properties (including the heat conduction) of complex materials can be studied at low temperature. Due to the submicron size of the nanocrystals, high-spatial-resolution measurements can be obtained. Alternatively, in the type-II configuration (see Sec. III C), the heating laser remains static, focused at a specific position on the surface. A large number of DBT-Ac nanocrystals distributed at random distances from the fixed heating source in combination with wide-field excitation allows for spatial mapping of the temperature distribution on the sample surface. Consequently, a fluorescence map of all probed nanocrystals can be imaged on the EMCCD camera as a function of the scanning frequency of the excitation laser, yielding a spatial map of the ZPL of each molecular thermometer. By construction, the proposed thermometer shows unmatched performance in terms of spatial resolution, low invasiveness, and working-temperature range, although it has a

limited temporal resolution. With regard to the temporal resolution, each measurement requires the recording of a spectroscopic trace, which generally takes a time of the order of 10 s, limiting the sampling rate to around 0.1 Hz. Although the scan speed, frequency range, and pumping power are chosen to guarantee minimum time consumption for optimal resolution, we consider our thermometer as a tool for steady-state measurements.

III. RESULTS AND DISCUSSION

A. Characterization of low-temperature single-molecule thermometers

A typical example of the thermometer calibration is reported in Fig. 2. In Fig. 2(a), excitation spectra are shown for a single DBT molecule on a flat silicon surface at different temperatures, with the red-shifted fluorescence intensity plotted as a function of the laser detuning to the ZPL ($\Delta\omega = \omega_{\mathrm{ZPL}} - \omega_L$). The molecule is excited confocally below saturation with a laser power, measured at the back entrance of the objective, $P = [0.3 - 5]$ nW, as the temperature increases from $T = 2.8$ to 11 K. A clear broadening of the line width with increasing cryostat temperature is observed. The dashed line shows a representative fit of the measurement to a Lorentzian peak. The measurements are repeated for different molecules and sample surfaces to extract the specific associated calibration curves (FWHM versus temperature). The results for gold, silicon, and a patterned silicon membrane are reported in Fig. 2(b), covering the temperature range from 2.8 to approximately 30 K. As the temperature increases, the excitation power is also increased up to several tens of nanowatts, in this way maintaining a constant excitation efficiency. Each surface presents a different upper temperature limit due to the related excitation and collection efficiency, which determine the attainable signal-to-noise ratio. Additional examples of calibration curves on silicon for different nanocrystals and different molecules in the same nanocrystal are provided in Appendix E (see Fig. 8). The experimental data (scattered points) and error bars are obtained as the average value and standard deviation, respectively, of the

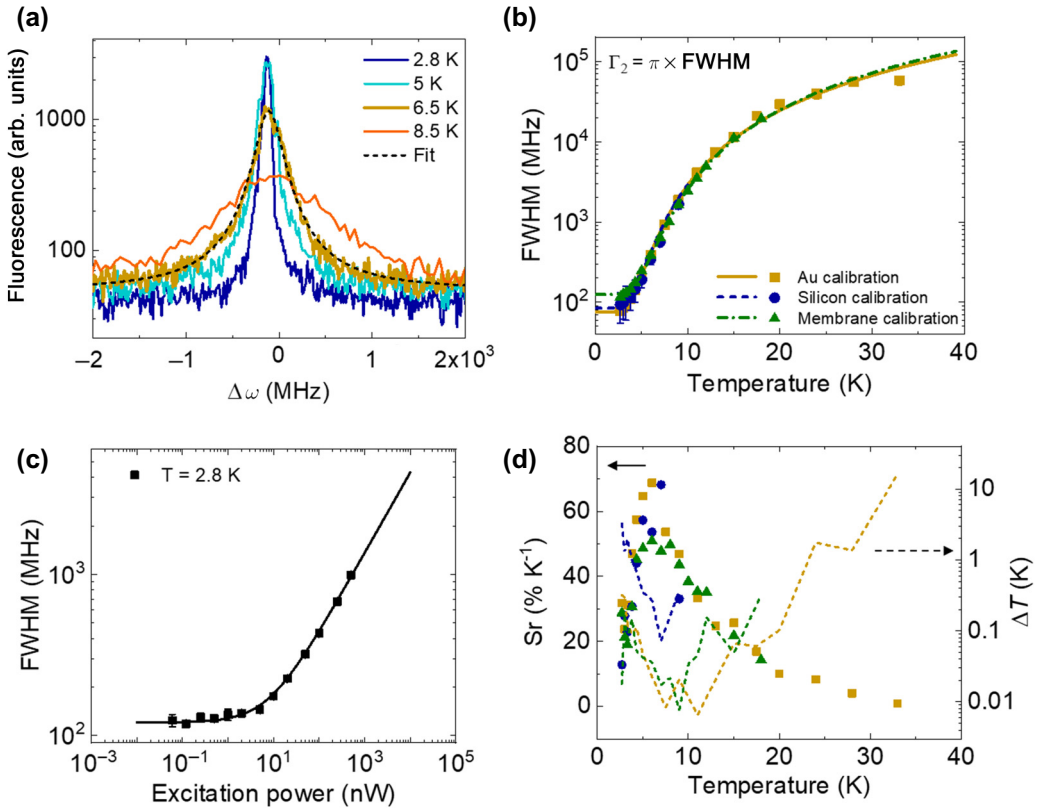

FIG. 2. The performance of a DBT-Ac nanocyrstal as a thermometer. (a) The intensity of the Stokes-shifted emission of a DBT-Ac nanocrystal on a silicon substrate as a function of the frequency detuning ($\Delta\omega$) between the excitation laser and the molecule ZPL for different sample temperatures. The dashed line displays a representative fit of the measurement to a Lorentzian peak. (b) Calibration curves, i.e., line width versus sample temperature, on gold (yellow), silicon (blue), and a patterned silicon membrane (green). The scattered points show the experimental measurements with error bars and the dashed and solid lines display the best fits to $\Gamma_2(T) = \Gamma_1/2 + \Gamma_2^*(T)$ with $\Gamma_2^*(T)$ given by Eq. (1). (c) The power dependence of the line width at $T = 2.8$ K. (d) The thermometer relative sensitivity (S_r, scattered points) and temperature resolution (ΔT, dashed lines) as a function of the temperature [colors as in (b)].

Lorentzian FWHM over at least four repeated excitation spectra. The best fit to the data is plotted in solid lines with the expression from Ref. [44], $\Gamma_2(T) = \Gamma_1/2 + \Gamma_2^*(T)$, where $\Gamma_2 = \pi \times \tilde{\gamma}$, $\Gamma_1 = 1/\tau_1$ (which is largely temperature independent) and $\Gamma_2^*(T)$ is the phonon-induced pure dephasing contribution. Clear *et al.* [44] have found that the latter can be expressed as

$$\Gamma_2^*(T) = \mu \int_0^\infty d\omega\, \omega^6 n(\omega)(n(\omega)+1) \times \int_0^\pi d\theta\, \sin(\theta)(1+\cos(\theta))^4 e^{-2\omega^2(1+\cos(\theta))/\xi^2}, \quad (1)$$

where $n(\omega)$ is the Boltzmann phonon distribution function for a given frequency ω and θ is the angle between two phonon wave vectors. The above expression has been specifically developed to include the electron-phonon interaction in the context of molecular crystals. Assuming that Γ_1 is approximately π times the FWHM at the lowest temperature measured ($T = 2.7$ K), the calibration can be fitted with two fitting parameters, μ and ξ, which correspond to the amplitude and to the phonon cutoff frequency, respectively.

Interestingly, the fitting of the calibration curve for NCx on the three different surfaces yields similar values for μ and ξ [$\mu = (6.3 \pm 0.8)10^{-6}$ ps^5, and $\xi = (6.1 \pm 0.3)$ ps^{-1}], as reported in Table I In the case of multiple probes, this allows us to use a single calibration curve at the cost of slightly lower accuracy. The optimal operating temperature range will always depend on the signal-to-noise ratio, which is higher for the molecules on gold among the cases examined in Fig. 2, for the reasons discussed in, e.g., Ref. [48].

The characteristic saturation behavior of the system is captured in Fig. 2(c), showing the line width as a function of the excitation power in confocal excitation at 2.8 K. The data are fitted to $\Gamma_2(P) = \Gamma_2\sqrt{1 + (P/P_S)}$, which yields a typical saturation power $P_S = (7.8 \pm 0.6)$ nW. All measurements presented in this work, notably those on silicon interfaces, employ laser powers $\leq$5 nW for the confocal configuration. These low power values ensure that the emission line width is not power broadened, representing a record-low operating power level, and consequently low invasivity, for all-optical temperature measurements.

The main figures of merit for thermometers are the sensitivity and temperature resolution [20,49]. A relative sensitivity can be defined as $S_r = (1/\gamma)(d\gamma/dT) \times 100$, expressed in % K^{-1}, where $\gamma =$ FWHM is used as the indirect measurement of temperature. Figure 2(d) summarizes the experimental (scattered points) sensitivities for three different surfaces. Regardless of the measured surface, the maximum S_r is found around 5–7 K, reaching up to $\simeq$70% K^{-1}, which, to our knowledge, is the highest S_r reported for all-optical thermometers (see, e.g., Refs. [9,50]), especially in this range [51].

The dashed lines in Fig. 2(d) correspond to the temperature resolution ΔT, given by the expression $\Delta T = \Delta\gamma(d\gamma/dT)^{-1}$, where $\Delta\gamma$ is the experimental error bar on the line width at a given temperature (obtained as described above). Consequently, ΔT is a measure of the minimum change in temperature that this technique can resolve. Depending on the substrate, this varies from 0.01 to 0.1 K over the temperature range 5–10 K, where the slope ($d\gamma/dT$) is steeper, being among the best temperature resolutions reported at the nanoscale [9]. Finally, the spatial resolution is given by the size of the nanocrystals, which is on average only a few hundreds of nanometers (see Ref. [39]), providing fine-grained access to local values of temperature and temperature gradients. The overall performance of the molecular thermometer makes it an excellent candidate for measuring heat transport under relevant environmental conditions, particularly those in which non-Fourier diffusion of heat is predicted to occur. This phenomenon tends to be difficult to investigate due to the characteristic low-temperature range and the fragility of samples [16].

B. Measurements of heat propagation in nanopatterned silicon membranes

As a representative example of a more complex surface, we study heat propagation in a phononic crystal. In particular, the device is a suspended silicon membrane with shamrock-shaped holes arranged in a periodic triangular lattice. Such patterns have commonly been used to control vibrations in solids and to prevent the propagation of specific phononic frequencies, which can be unwanted sources of noise and dephasing in quantum systems [52–54]. Figure 3(a) displays a sketch of the sample geometry with the corresponding values for the thickness of the patterned membrane (250 nm), the silicon substrate (600 μm), and the space between the membrane and substrate (nominally 3 μm). The cross-section view also shows a generic position of both lasers. Specifically, we consider a suspended silicon membrane of size 63 μm × 63 μm with a nonpatterned suspended silicon frame of width 6 μm (see the inset on the left). SEM images of the shamrock-shaped pattern with a periodicity of 400 nm and a fill fraction of approximately 60% are shown as insets to the figure (see details on the geometry in Ref. [54] and about fabrication in Appendix A).

The inset in Fig. 3(b) shows the measurement configuration, as described in Sec. B: the heating laser (yellow light) moves along a line containing the selected molecular thermometer (the red disk), whereas the ZPL line width is estimated via excitation spectroscopy. The obtained values are plotted in Fig. 3(b) as a function of the relative distance between the DBT molecule and the position of the heating

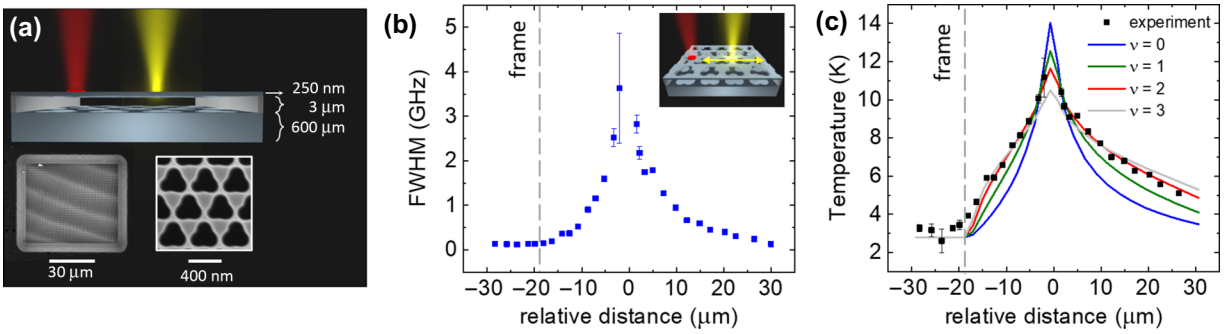

FIG. 3. The temperature profile on a silicon-patterned membrane. (a) A sketch of the sample cross section with the heating and probe laser (yellow and red beam, respectively). The insets at the foot show scanning-electron-microscope (SEM) images of the sample: the complete membrane (shown in the left inset) depicts the surrounding frame, while the shamrock-shaped pattern is visible in the right inset. (b) The line width versus the relative distance between the moving heating laser and the DBT-Ac nanocrystal. The error bars correspond to repeated laser scans as explained in Sec. III A. The inset shows a schematic of the measurement configuration, with the fixed probe laser on the NCx (the red disk on the surface of the sample) and the displacing heat source. The dashed vertical line indicates the frame position. (c) The temperature profile as a function of the relative distance. The black squares denote temperatures estimated from experimental measurements in (b), considering a calibration curve as described in Sec. III A. The solid lines represent the calculated temperature profiles assuming different power laws (ν) for the dependence of the thermal conductivity on the temperature [see Eq. (F4)].

laser. Clearly, the line width broadens as the heating laser approaches the DBT molecule. It is worth noting that the nanocrystal is around 20 μm away from the frame (indicated with a dashed vertical line), which can be considered as a thermal sink, explaining the asymmetric shape of the profile.

In order to interpret the experimental results, we solve the heat equation by considering a nonconstant thermal conductivity, consistent with both Debye's and Einstein's model for the heat capacity at cryogenic temperatures. The temperature dependence of the thermal conductivity, in this range of temperatures, is assumed to be of the form $\kappa \sim T^{\nu}$, where ν is the exponent of the power law [55]. A fixed-bath-temperature boundary condition of 2.8 K is considered outside the rectangular membrane (for further details, see Appendix F). The theoretical results are then compared with the experimental data of the temperature as a function of the position of the heat source in Fig. 3(c). The black squares correspond to the temperature values estimated from the experimental points in Fig. 3(b), using a calibration curve specific for that NCx and fitted assuming the values of μ and ξ as described in Sec. III A. The zero-temperature line width $\Gamma_1/2\pi$ is 120 MHz and corresponds to the off configuration of the heating laser. The solid lines show the calculated temperature profile, assuming a power-law dependence of the heat conductance with temperature for different values of ν. The blue line displays the best fit for the theoretical profile assuming a constant thermal conductivity 0.0084 ± 0.0006 W/(m K).

We find that the best fit to our experimental results corresponds to an exponent $\nu = (2.1 \pm 0.1)$, showing excellent agreement and leading to a sample thermal conductivity of (0.0032 ± 0.0001) W/(m K) at 4 K. This estimate is based on the assumption of 1% absorption of the impinging power, which is based on the transfer-matrix method in the multilayer structure, considering the optical properties of silicon at room temperature (from Ref. [56]). Interestingly, the value $\nu = 2$ is associated with heat propagation in two dimensions, which is expected for a suspended membrane. In Appendixes C and D, we also successfully compare simulations and experiments for the case of a broken membrane and a silicon slab. Moreover, our estimation of κ is in accordance with values in the literature for nanostructured silicon membranes at 4 K [57–62]. These findings validate our molecular two-level system as a high-sensitivity thermometer, allowing for measurements in complex samples at cryogenic conditions.

C. 2D temperature mapping at 3 K with multiple quantum thermometers

The ability to simultaneously measure temperature at different positions on a surface in principle allows for the heating and dissipation processes to be studied as a whole, rather than locally, which significantly reduces the acquisition time. Toward this goal, the type-II experimental configuration [see Fig. 4(a)] is applied to the suspended membrane characterized in Sec. III B, with a large number of doped Ac crystals deposited via drop casting (for more details, see Appendix A). The inset shows a schematic of the measurement configuration in which the heating laser (yellow beam) remains static while the excitation laser (expanded red beam) allows the collection of fluorescence (red dots) from several molecular thermometers (red disks on the surface) simultaneously, providing a temperature map of the sample. In Fig. 4(a), the scattered

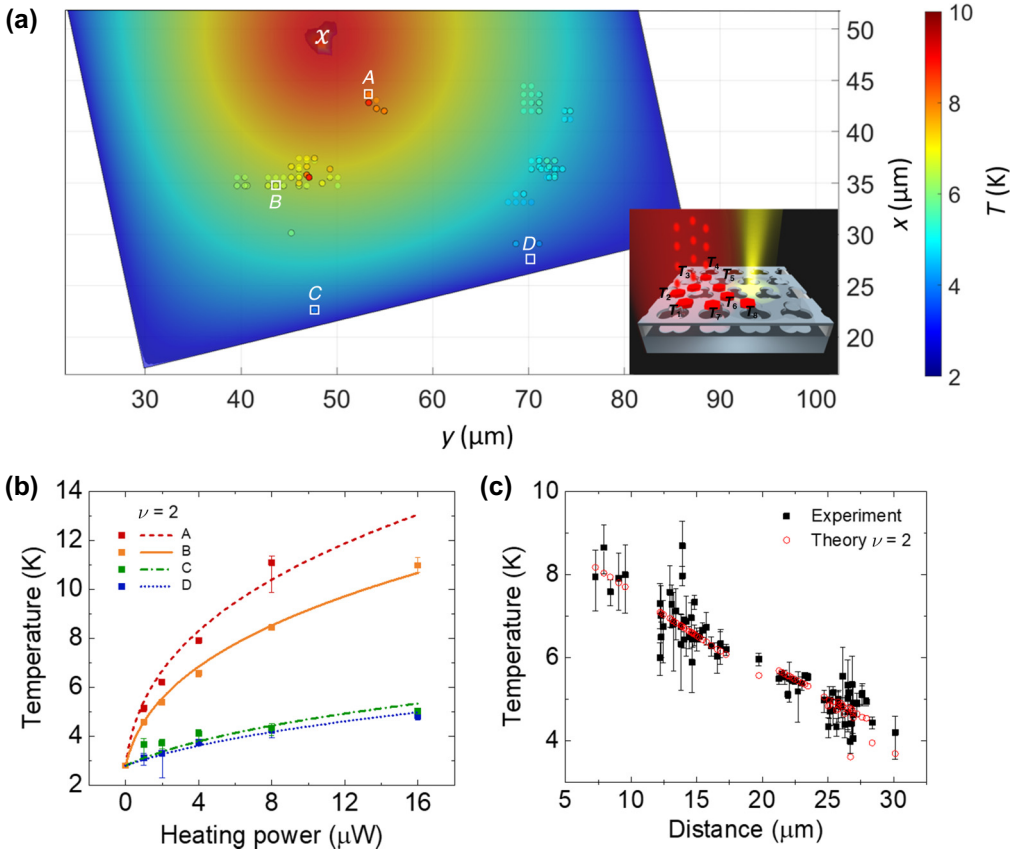

FIG. 4. 2D temperature mapping on a patterned silicon surface. (a) The measured and calculated temperature profiles (color scale) for the suspended membrane also analyzed in Fig. 3. The experimental points are highlighted with circles. The position of the heating laser is indicated with a white x. The inset shows a schematic of the measurement configuration, in which the heating laser (yellow beam) remains static while the excitation laser (expanded red beam) allows for the collection of fluorescence (red dots) from several molecular thermometers (red disks on the surface of the sample) simultaneously, providing a temperature map of the sample. (b) The dependence of the temperature on the heating-laser power for four DBT-Ac nanocrystals, labeled as A, B, C, and D, positioned as highlighted in (a) [see Eq. (F4)]. (c) The temperature as a function of the DBT-Ac nanocrystal distance with respect to the heating source at 4-μW heating-laser power. The black squares correspond to experimental data, whereas the red circles denote the calculated temperature, assuming $\nu = 2$.

points illustrate the nanocrystal positions, together with the extracted temperature represented by the color scale, obtained using localization techniques and excitation spectroscopy, this time performed using the EMCCD camera. The calculated temperature distribution over the membrane is also reported, using the same color scale. The measured temperature values closely follow the calculated temperature profile. This validates our mapping of the temperature profile with discrete sampling and high spatial accuracy in a temperature range around 5 K.

As representative cases, we select four DBT-Ac nanocrystals, labeled A, B, C, and D, for further analysis (highlighted with white squares). These are 8.9, 19.2, 33.1, and 37.9 μm away from the heating source, respectively. Figure 4(b) displays how the temperature behaves differently as a function of the heating-laser power in such locations. In particular, the closer the DBT-Ac is to the heat source, the stronger is the temperature power dependence. The experimental data (scattered points) are fitted according to the calculated power dependence, assuming $\nu = 2$.

In addition, Fig. 4(c) presents the temperature estimated using 81 DBT-Ac nanocrystals as a function of their distance from the heat source, operated with a laser power of $P_H = 4$ μW. The large number of temperature sensors on the surface allows for the reconstruction of a well-defined temperature profile showing the characteristic length scale of thermal transport on this surface, which is consistent with 2D heat propagation. Remarkably, the characteristic length scale is larger compared to Fig. 7(f), which displays measurements on a nonsuspended membrane. This means that, in the latter, the heat propagation is not just along the membrane, i.e., the temperature drops more steeply because heat can also flow toward the bottom of the sample. In Fig. 4, the fluctuations are largely a result of weak signals in some of the molecules leading

to small deviations of the specific calibration curve from the assumed one, or disorder introduced by imperfections on the surface. In addition, other effects such as non-Fourier heat propagation and the Casimir-Knudsen edge effect can potentially affect the thermal conductivity and the temperature distribution in our geometry. However, measuring those effects would require further systematic analysis beyond the scope of this work.

IV. CONCLUSIONS

We have presented a single-molecule thermometer that allows for the measurement of temperature via the broadening of the zero-phonon transition line in a temperature range from 3 to 20 K. Our nanoscopic thermometers, DBT molecules embedded in anthracene nanocrystals, exhibit a relative sensitivity of 70% K^{-1} around 5 K, a thermal resolution ranging from 0.1 to 0.01 K, and a spatial resolution of a few hundreds of nanometers, given by the size of the probes. Furthermore, the thermometer operates at low power, less than 5 nW, which marks a record-low impact in this temperature range. We have demonstrated the potential of our nanoprobe by performing 2D temperature mapping of a nanostructured surface and we have validated the results against theoretical calculations. We observe the characteristic heat-propagation regime in a patterned silicon membrane. These results pave the way for using molecules as probes for the thermal properties of materials, going beyond the Fourier-diffusion theory of phonon propagation, given the operating temperature range of a few kelvin, the possibility of performing 2D temperature maps, and the feasibility of working with nanostructured samples.

ACKNOWLEDGMENTS

We would like to thank Prof. Michel Orrit and Robert Smit for providing us the dibenzoterrylene molecules. This work is Co-funded by the European Union (ERC, QUINTESSEnCE, 101088394). Views and opinions expressed are however those of the author(s) only and do not necessarily reflect those of the European Union or the European Research Council. Neither the European Union nor the granting authority can be held responsible for them. It was funded by the the EC under the FET-OPEN-RIA project STORMYTUNE (G.A. 899587), from the EMPIR programme (project 20FUN05, SEQUME), co-financed by the Participating States and from the European Union's Horizon 2020 research and innovation program. Also financial support has been received from: PNRR MUR project PE0000023-NQSTI. V.E. acknowledges funding from European Union (NextGenerationEU), the Ministerio de Universidades of Spain, and the University of Seville under the Grant Margarita Salas. R.C.N. acknowledges funding from the EU-H2020 research and innovation program under the Marie Sklodowska Curie Individual Fellowship (Grant No. 897148). ICN2 is supported by the Severo Ochoa program, the Spanish Research Agency (AEI, grant no. SEV-2017-0706) and the CERCA Programme/Generalitat de Catalunya.

C.T. conceived the research. V.E. and R.D. performed the experiments, while M.H. developed the theoretical model and performed data analysis together with V.E. and R.D. The samples were prepared by R.N. and G.A., under the supervision of P.G. and C.S.T. P.L. helped with the optical setup and E.C.A. discussed the theory of thermal conduction. V.E. and C.T. wrote the paper, with critical feedback from all authors. The figures were prepared by M.C.

Note added.—We have recently become aware of related work in Ref. [51], where the authors have used a single negatively charged germanium vacancy (GeV) color center in nanodiamonds as a temperature probe, attaining a sensitivity of approximately 20% K^{-1}.

APPENDIX A: METHODS

1. Preparation and deposition of DBT-Ac nanocrystals

The DBT-Ac nanocrystals were formed in aqueous suspension. 50 μL of a $1:10^7$ mixture of 1 mM DBT in toluene and 5 mM Ac in acetone solution was injected into 2 ml of Milli-Q® water and sonicated for 30 min. The solvents and Ac were purchased from Sigma-Aldrich, the water was deionized by a Milli-Q® Advantage A10 system (18.2 mΩ cm at 25°), and the DBT (>90% pure) was obtained by custom synthesis performed by the Dutch company Mercachem, nowadays called Symeres. The resulting nanocrystals were then deposited on the surface of interest via drop casting. In this technique, a drop of 20 μl of the suspension is deposited on the surface, followed by a desiccation procedure assisted with vacuum at room temperature, resulting in the deposition of several hundreds of nanocrystals.

2. Patterned-silicon suspended membrane preparation

The suspended shamrock crystal membranes were fabricated on a silicon-on-insulator (SOI) platform using conventional nanofabrication techniques. The SOI chips initially underwent an O_2 plasma treatment in an inductively coupled plasma reactive-ion etcher (ICP RIE) at relatively low powers (400 W) for 1 min to enhance the surface adhesion of the subsequent resist. CSAR 62 (AR-P 6200.09) positive-tone electron-beam resist was spun onto the surface at 4000 rpm for 1 min and then postbaked at 150 °C for 1 min. Shamrocks were patterned into the resist using a 30-kV Raith electron-beam system and then developed for 1 min in AR-600-546 developer. The development was stopped after 30 s in AR-600-60 stopper, followed by 30 s in isopropanol. The pattern was transferred into the device layer using a pseudo-Bosch ICP-RIE etch. A low-power

O_2 etch in the ICP RIE was also able to strip away any residual resist following the silicon etch. Finally, the membrane was suspended in a 3-min 50% hydrofluoric acid etch, followed by critical-point drying.

APPENDIX B: SINGLE-PHOTON EMITTER MOLECULAR THERMOMETER

DBT molecules embedded in anthracene NCx are well-known single-photon emitters and are widely used for quantum photonics applications. In this experiment, we also perform a measurement of the intensity autocorrelation function ($g^{(2)}$) in a Hanbury Brown–Twiss configuration. Figure 5 shows the experimental data in black, whereas the red solid line represents the fitting to a single exponential, leading to $g^{(2)}(0) = 0.02 \pm 0.04$ and correlation time $\tau_1 = 3.5 \pm 0.2$ ns. The observed antibunching dip shows that we can easily isolate a single-quantum emitter within each nanocrystal, with the resonant pumping scheme employed throughout this work.

APPENDIX C: TEMPERATURE PROFILE OF A BROKEN MEMBRANE

The method described in Sec. III B to measure the temperature profile on a surface can be extended to even more complex systems. For instance, with the nanothermometers presented in this work, we were able to realize temperature measurements on a broken membrane, as we show in Fig. 6.

The nanocrystals were deposited on the membrane by microinfiltration. With this technique, a few nanocrystals can be released using a setup (Eppendorf Femtojet) that consists of a micropipette (Eppendorf Femtotips) with an external diameter of about 2 μm and an inner diameter of 0.5 μm, held on a three-dimensional micrometeric stage for fine movement. The aqueous suspension of nanocrystals (for the synthesis of DBT-Ac nanocrystals, see Appendix A) is injected into the micropipette and the tip is brought close to the region of interest until a microdrop of suspension is deposited via surface adhesion, with high spatial resolution.

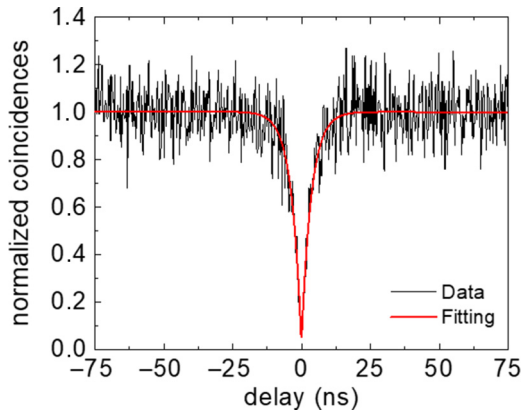

FIG. 5. A histogram of the relative arrival time between the two SPADs in the Hanbury Brown–Twiss configuration. The solid red line is a single exponential fit to the data, yielding $g^{(2)}(0) = 0.02 \pm 0.04$ and $\tau_1 = 3.5 \pm 0.2$ ns.

Figure 6(a) shows a sketch of the sample geometry with the corresponding thicknesses of the patterned membrane (250 nm), the silicon substrate (600 μm), and the space between the suspended membrane and the substrate (nominally 3 μm). As in Fig. 3, the cross-section view also shows generic positions of the two lasers. Specifically, we consider a broken suspended silicon membrane of size 50 μm × 40 μm with a nonpatterned suspended silicon frame of width 4.5 μm (see the inset on the left). The shamrock-shaped pattern with a periodicity of 500 nm and a fill fraction of approximately 50% is depicted in the inset on the right (see details on the geometry in Ref. [54] and more details of fabrication in Appendix A).

The inset in Fig. 6(b) shows the measurement configuration, as described in Sec. B. The obtained line widths are plotted in Fig. 6(b) as a function of the relative distance between the DBT molecule, i.e., the molecular thermometer, and the position of the heating laser. As in Fig. 3(b), the line width broadens as the heating laser comes closer to the DBT molecule. It is worth noting that the DBT molecule is only 5 μm away from the frame (which can be considered to be a thermal sink) and also the fact that in this specific case, the membrane has ruptured during the nanocrystal deposition, resulting in a tear 20 μm away from the molecular thermometer [both distances are highlighted in Fig. 6(b) with a vertical dashed blue line and respective labels]. These two factors are what give rise to the asymmetric shape of the line-width profile.

To interpret the experimental results, the heat equation is solved numerically because of the complex boundary. An extra boundary condition is considered for the tear, which considers a vanishing heat flux at the tear. The results of the numerical simulation are then compared to the experimental data of the temperature as a function of the position of the heat source in Fig. 6(c). The red circles correspond to the temperature values estimated from the experimental points in Fig. 6(b), assuming the calibration curve described in Sec. III A with a lifetime-limited line width $\Gamma_1/2\pi = 196$ MHz, which was obtained with the heating laser off. The lines show the simulated temperature profile assuming the power-law dependence of the heat conductance with the temperature. The dashed gray and dashed-dot black lines display the theoretical profile with constant thermal conductivity 0.005 W/(m K). Additionally, the former includes the boundary condition due to the tear, whereas the latter assumes no tear, i.e., that the membrane is not ruptured. All other T^{ν} curves take into account the presence of a tear.

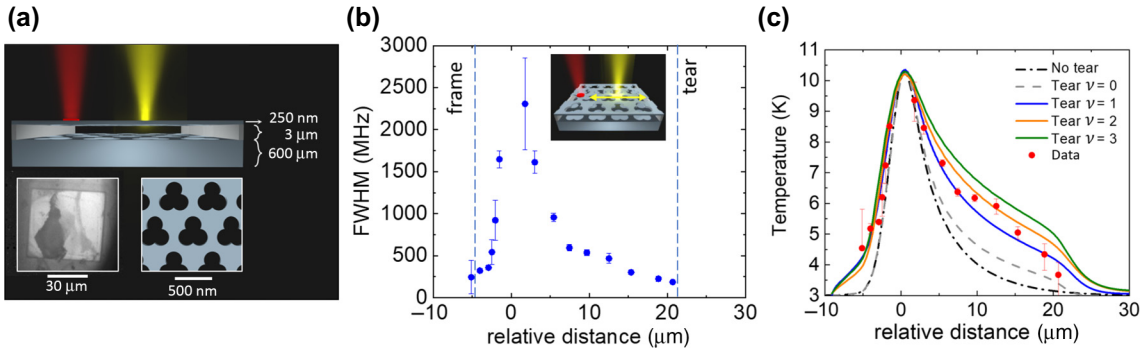

FIG. 6. The temperature profile on a broken patterned silicon membrane. (a) A cross section of the sample indicating the thickness of the membrane, the substrate, and the space between them, together with a representative placement of the position of the lasers (red and yellow beams). An SEM image of the complete membrane reveals the frame surrounding the membrane in the inset on the left. The inset on the right shows the shamrock-shaped pattern of the membrane. (b) The line width versus the relative distance between the moving heating laser and the DBT-Ac nanocrystal. The error bars correspond to repeated laser scans, as explained in Sec. III A. The inset shows a schematic of the configuration in which the measurements are taken, interrogating only one nanocrystal while displacing the heat source. In addition, the dashed vertical lines indicate the location of the frame and the tear with respect to the position of the nanocrystal. (c) The temperature profile as a function of the relative distance between the moving heating laser and the DBT-Ac nanocrystal. The red circles denote temperatures estimated from experimental measurements in (b) considering a calibration curve as described in Sec. III A. The solid lines represent simulated temperature profiles assuming different power laws of dependence of the thermal conductivity on the temperature, as well as the presence or lack thereof of the tear, as described in the text.

We find that the power laws that best fit our experimental measurements correspond to an exponent ranging from $\nu = 1$ to $\nu = 2$. The estimation of the sample thermal conductivity at 4 K for $\nu = 1$ and $\nu = 2$ is (0.0032 ± 0.0006) W/(m K) and 0.0015 ± 0.0003 W/(m K), respectively, estimating a 1% absorption of the impinging power. This percentage has been determined using the transfer-matrix method in the multilayer structure shown in Fig. 6(a), employing the optical properties of silicon at room temperature from Ref. [56]. Our estimation of κ is in accordance with values in the literature for nanostructured silicon membranes at 4 K [57–62].

APPENDIX D: HEAT PROPAGATION ON A NONSUSPENDED MEMBRANE

Type-II measurements were also performed on a nonsuspended pattesrned silicon membrane, using a heating laser of wavelength 767 nm. The inset in Fig. 7(a) shows an SEM image of the nanostructured SOI surface, which is characterized by circular holes 45 nm in radius, 250 nm deep with a 500 nm periodicity, and with a fill fraction of approximately of 15% (the scale bar is 200 nm). In Fig. 7(b), an optical-microscope image demonstrates how the NCx spread all over the nonsuspended membrane that we study (indicated with a black arrow), covering the whole area right after the deposition (via drop casting) and before the cool-down process. During the process of cooling the sample down, some of the NCx sublimates due to the pressure conditions. Despite this fact, we still find enough NCx emitting from the substrate at cryogenic temperatures to perform type-II measurements. Figure 7(c) shows the SEM image of the nonsuspended membrane after extracting the sample from the cryostatic chamber once the measurements have been performed. It is possible to observe only a few big crystals since most of the NCx sublimate during the heating procedure to remove the sample from the cryostat. Figure 7(d) illustrates the nanocrystal positions with the related temperature estimation as obtained using localization techniques and excitation spectroscopy performed with the EMCCD camera (as a guide for the eye, the corner of the structured area on the sample is denoted with white dashed lines). The laser heat source is then kept at a fixed position, marked with a yellow dot, which is placed at a varying distance from the various crystals. This clearly shows the possibility of mapping temperature profiles with discrete sampling and high spatial accuracy around the 5 K range.

As representative cases, we select four DBT-Ac nanocrystals, labeled *A*, *B*, *C*, and *D*, for further analysis. These are 6.3, 12.7, 25.7, and 34.0 μm away from the heating source, respectively. Figure 7(e) shows how the line width of these molecules behaves differently as a function of the heating-laser power. In particular, the closer the DBT-Ac is to the heat source, the stronger the molecule ZPL line width scales with power. In these measurements in which the heating wavelength is closer to the ZPL, as the heating-laser power increases, two effects lead to an increase in the size of the error bars: the corresponding temperature increase broadens the line and decreases its amplitude as the Debye-Waller factor diminishes. While the signal decreases, the background increases due to laser leakage and possible residual excitation of the probed molecule via the transition to the

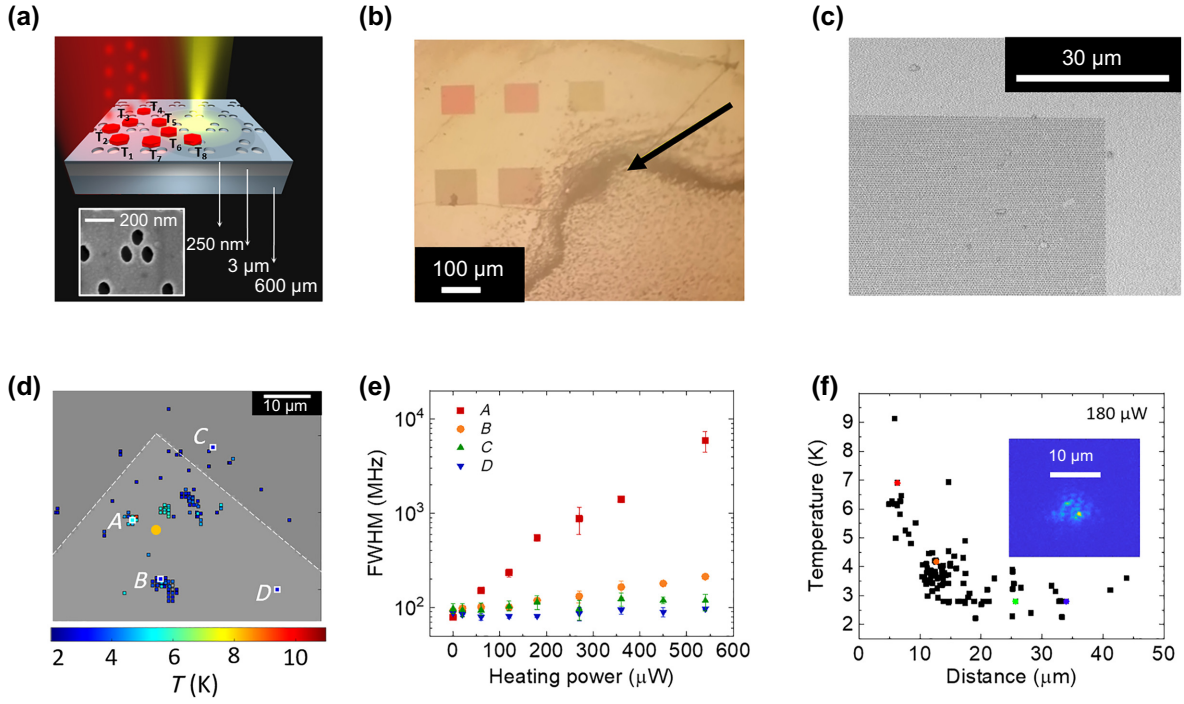

FIG. 7. 2D temperature mapping on a nonsuspended patterned silicon surface. (a) A schematic of the measurement configuration, in which the heating laser (yellow beam) remains static while the excitation laser (expanded red beam) allows collection of the photoluminescence (red spots of light) of several molecular thermometers (red hexagonal crystals on the sample) simultaneously, providing a temperature map of the sample. The sample consists of a SOI substrate with a 250-nm-thick silicon device layer with the pattern shown in the inset in a SEM image, a 3-μm silicon dioxide buried oxide middle layer, and a 600-μm silicon substrate. (b),(c) Optical microscope (b) and SEM (c) images before and after performing measurements in the cryostat, respectively. (d) A top view of a corner of the patterned silicon surface. The heating laser and DBT-Ac nanocrystals are represented by a yellow circle and small squares, respectively. The color scale denotes the temperature measured by each molecular thermometer on the sample surface. (e) The dependence of the line width on the heating-laser power for four DBT-Ac nanocrystals, labeled as A, B, C, and D, highlighted in white in (d). (f) The temperature as a function of the DBT-Ac nanocrystal distance with respect to the heating source at a given heating power of 180 μW. The colored squares correspond to labeled nanocrystals in (e) with the same color code. The inset shows the speckle pattern of the heating laser on the sample surface.

higher vibrationally excited state (0-1), beyond the probed ZPL (0-0). We point out that this effect is due to the specific heating mechanism that is used here to prove the principle and that is in essence not related to the sensing device. As described in Sec. III A, measuring $\Gamma_1 = 1/\tau_1$ of each nanocrystal with a unique frequency scan of the resonant laser in wide-field illumination and imaging the sample on the camera determines the calibration curve for each DBT-Ac nanocrystal given the parameters μ and ξ in Eq. (1). Figure 7(f) presents the temperature estimated using tens of DBT-Ac nanocrystals as a function of their distance from the heat source, operated with a laser power $P_H = 180$ μW. Nanocrystals A, B, C, and D are highlighted with their corresponding colors in Fig. 7(e). The large number of temperature sensors on the surface allows for a reconstruction of a clear temperature profile showing the characteristic length scale of thermal transport on this surface. In this regard, the characteristic length scale is lower compared to Fig. 3(c) as the structure is not suspended and behaves as bulk. The scattering of the data should be ascribed to the speckle pattern produced by the heating laser on the surface [see inset in Fig. 7(f)], which induces spatial fluctuations of the temperature.

APPENDIX E: EXAMPLES OF FITTING OF CALIBRATION CURVES ON DIFFERENT SUBSTRATES AND CALIBRATION CURVES OF DIFFERENT MOLECULES ON SILICON

Table I shows the values of the fitting parameters for the different material surfaces used in this work. Since the μ and ξ parameters are connected and variations in one of them imply variations in the other, here we have fixed the value of $\xi = (6.1 \pm 0.3)$ ps^{-1}. This value was obtained by fitting the molecule on the gold substrate, which was measured over the widest temperature range (2.7–33 K). The average value of $\mu = (6.3 \pm 0.8) \times 10^{-6}$ ps^5, together with $\xi = 6.1$ ps^{-1}, will be used for estimating the calibration curves of any molecule given that Γ_1 is known for each one from the off configuration of the heating-laser

TABLE I. The values of the fitting parameters in Eq. (1) for the experimental calibration curves measured on different substrates.

Material	Γ_1 (MHz)	μ (ps^5)	ξ (ps^{-1})
Gold	(76 ± 11)	$(7.1 \pm 0.6) \times 10^{-6}$	(6.1 ± 0.3)
Silicon	(92 ± 6)	$(5.4 \pm 0.4) \times 10^{-6}$	6.1
Membrane	(118 ± 6)	$(6.3 \pm 0.2) \times 10^{-6}$	6.1

measurements. Regardless of the parameters from Table I used for μ, the calibrated temperatures differ by less than 5% over the experimental range.

The DBT molecules inside the anthracene NCx can be accommodated in the crystalline host matrix at different positions and relative angles with respect to the axis of the lattice structure. This fact, together with the existence of lattice defects, trapped charges, etc., modifies the environment surrounding each DBT molecule and affect the emission of each molecule. Such an effect can be noted in Fig. 8, where the experimental calibration curves (scattered points) for three different molecules are displayed, showing that each molecule has a different value of $\Gamma_1/2\pi$. The solid lines represent the estimated calibration curve using $\mu = 6.3 \times 10^{-6}$ ps^5, $\xi = 6.1$ ps^{-1}, and the corresponding Γ_1 value for each molecule in $\Gamma_2(T) = \Gamma_1/2 + \Gamma_2^*(T)$ and Eq. (1). Note that molecules 1 and 2 are inserted in the same NCx, whereas molecule 3 is in a different NCx.

We can compare these parameters with those obtained by Clear *et al.* [44]. They obtained $\mu = 1.8 \times 10^{-6}$ ps^5 (corrected by a factor of 4 missing in their computation) and $\xi = 8.6$ ps^{-1}.

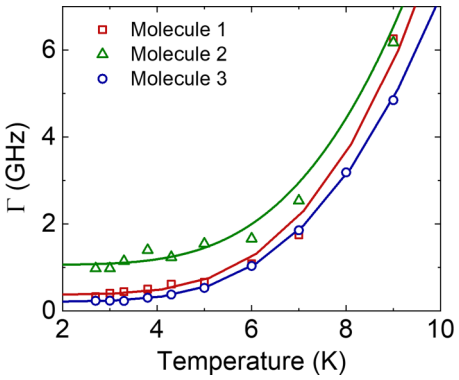

FIG. 8. Examples of calibration curves of different molecules on a silicon substrate. The scattered points represent the experimental data, whereas the solid lines correspond to fitting curves according to $\Gamma_2(T) = \Gamma_1/2 + \Gamma_2^*(T)$ and Eq. (1). The fixed values of parameters μ and ξ are 6.3×10^{-6} ps^5 and 6.1 ps^{-1}, respectively, which are the same values as in the main text.

APPENDIX F: THEORY AND NUMERICAL SIMULATION OF HEAT TRANSPORT IN 2D MEMBRANES

In two dimensions, the heat equation can be written as

$$\frac{\partial \kappa(x,y)}{\partial x}\frac{\partial T(x,y)}{\partial x} + \frac{\partial}{\partial y}\kappa(x,y)\frac{\partial T(x,y)}{\partial y} + \dot{Q}(x,y) = \rho c \frac{\partial T(x,y)}{\partial t}, \tag{F1}$$

where κ is the thermal conductivity, $\dot{Q}$ is the heat-generation rate, ρ is the mass density, and c is the heat capacity. For a uniform rectangular membrane of size $X \times Y$ attached to a heat sink on all four sides at temperature T_0 and assuming that the thermal conductivity of the membrane can be described by a power law, i.e., $\kappa(x,y) = \kappa_0 (T(x,y)/T_0)^\nu$ as expected at low temperatures [55], we can rewrite Eq. (F1) in thermal equilibrium as

$$\frac{\kappa_0}{(\nu+1)T_0^\nu}(\partial_x^2 + \partial_y^2) + T(x,y)^{\nu+1} + \dot{Q}(x,y) = 0, \tag{F2}$$

where $\partial_x^2 + \partial_y^2$ is the 2D Laplacian. At this point, we are also assuming that the presence of NCxs at the membrane surface is negligible, as their density implies an extrinsic scattering length much longer than the expected mean free path ($\simeq$250 nm; see, e.g., Ref. [63]). This equation can be solved for an arbitrary generation rate using the Green's function $G(x,y,x',y')$ of the 2D Laplacian with boundary condition $G(x,y,x',y') = 0$ for $x, x', y,$ or $y' = 0$ and x or $x' = X$ and y or $y' = Y$. The Green's function is then given by

$$G(x,y,x',y') = \frac{4}{XY}\sum_{n,m=1}^{\infty} \sin\left(\frac{\pi n x}{X}\right)\sin\left(\frac{\pi n x'}{X}\right) \times \sin\left(\frac{\pi m y}{Y}\right)\sin\left(\frac{\pi m y'}{Y}\right), \tag{F3}$$

which, for the temperature, yields

$$T(x,y)^{\nu+1} = T_0^{\nu+1} + \frac{T_0^\nu}{(\nu+1)\kappa_0}\int_0^X dx' \int_0^Y dy' \times G(x,y,x',y')\dot{Q}(x',y'). \tag{F4}$$

This is the expression used to compute the theoretical temperature profile shown in Fig. 4, where we have assumed a Gaussian profile for the heat-generation rate from the heating laser. The power dependence used in the main text can then be expressed as $T = (T_0^{\nu+1} + \alpha P)^{1/(\nu+1)}$, where P is the heating power and α is a coefficient that depends on the configuration.

For the case of the broken membrane, we cannot use Eq. (F4) because of the more complicated boundary condition along the broken membrane. Therefore, we directly

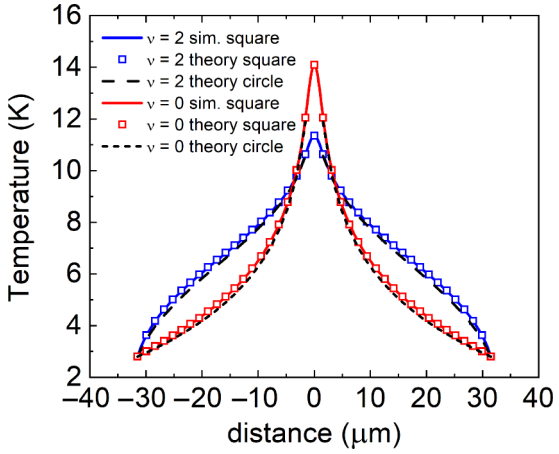

FIG. 9. The temperature as a function of the distance from the heater is shown for different values of the thermal conductivity exponent ν. The solid lines are the results of the simulations using Eq. (F5) and the squares and dashed lines represent the results of the theory evaluating Eq. (F4) for a square and a circular membrane, respectively. The parameters used are $\kappa_0 = 0.0084$ and $\kappa_0 = 0.00155$ for $\nu = 0$ and $\nu = 2$, respectively. We have further assumed a Gaussian heating profile at the center of power $1\% \times 4\ \mu$W and radius $1.5\ \mu$m. The membrane thickness has been assumed to be 250 nm.

solve the heat equation [Eq. (F1)] numerically using finite-difference methods. This equation can be solved iteratively by computing

$$T_{n+1}(\vec{r}) = \sum_{\hat{\delta}} \frac{\kappa_n(\vec{r}+\hat{\delta}) - \kappa_n(\vec{r}-\hat{\delta}) + 4\kappa_n(\vec{r})}{16K_n} T_n(\vec{r}+\hat{\delta}) + \left(1 - \frac{\kappa_n(\vec{r})}{K_n}\right) T_n(\vec{r}) + \frac{dx^2}{4K_n}\dot{Q}(\vec{r}), \tag{F5}$$

where T_n and κ_n are the temperature and thermal conductivity at time ndt, $(T_{n+1} - T_n) = dt\dot{T}$, $\hat{\delta} = \pm\vec{dx}$ and $\pm\vec{dy}$. We further assume that the discretizations in x and y are the same ($dx = dy$) and that $K_n = dx^2\rho c/4dt$. For fast convergence, we can choose $K_n = \max\{\kappa(x,y)\}$, which is computed at each time iteration. When $|T_{n+1} - T_n|$ is smaller than the desired uncertainty, the iteration is stopped. Note that because of the temperature dependence of the thermal conductivity κ, its value has to be computed at every iteration, which slows down the computation as compared to the case when κ does not depend on the temperature. Typically, graphics processing units were used in parallel was used to compute the time iterations. A comparison between the numerical iterative solution and the analytical one is shown in Fig. 9.

[1] A. Pasupathy, R. Velraj, and R. Seeniraj, Phase change material-based building architecture for thermal management in residential and commercial establishments, Renewable and Sustainable Energy Rev. **12**, 39 (2008).

[2] S. Yang, J. Wang, G. Dai, F. Yang, and J. Huang, Controlling macroscopic heat transfer with thermal metamaterials: Theory, experiment and application, Phys. Rep. **908**, 1 (2021).

[3] J. Zhang, D. Shao, L. Jiang, G. Zhang, H. Wu, R. Day, and W. Jiang, Advanced thermal management system driven by phase change materials for power lithium-ion batteries: A review, Renewable Sustainable Energy Rev. **159**, 112207 (2022).

[4] C.-P. Feng, F. Wei, K.-Y. Sun, Y. Wang, H.-B. Lan, H.-J. Shang, F.-Z. Ding, L. Bai, J. Yang, and W. Yang, Emerging flexible thermally conductive films: Mechanism, fabrication, application, Nano-Micro Lett. **14**, 1 (2022).

[5] J. Mathew and S. Krishnan, A review on transient thermal management of electronic devices, J. Electron. Packag. **144**, 010801 (2022).

[6] M.-D. Li, X.-Q. Shen, X. Chen, J.-M. Gan, F. Wang, J. Li, X.-L. Wang, and Q.-D. Shen, Thermal management of chips by a device prototype using synergistic effects of 3-D heat-conductive network and electrocaloric refrigeration, Nat. Commun. **13**, 1 (2022).

[7] Q. Chen, Z. Ma, Z. Wang, L. Liu, M. Zhu, W. Lei, and P. Song, Scalable, robust, low-cost, and highly thermally conductive anisotropic nanocomposite films for safe and efficient thermal management, Adv. Funct. Mater. **32**, 2110782 (2022).

[8] R. A. Lawag and H. M. Ali, Phase change materials for thermal management and energy storage: A review, J. Energy Storage **55**, 105602 (2022).

[9] C. D. Brites, P. P. Lima, N. J. Silva, A. Millán, V. S. Amaral, F. Palacio, and L. D. Carlos, Thermometry at the nanoscale, Nanoscale **4**, 4799 (2012).

[10] M. M. Kim, A. Giry, M. Mastiani, G. O. Rodrigues, A. Reis, and P. Mandin, Microscale thermometry: A review, Microelectron. Eng. **148**, 129 (2015).

[11] S. Jevtic, D. Newman, T. Rudolph, and T. M. Stace, Single-qubit thermometry, Phys. Rev. A **91**, 012331 (2015).

[12] J. Maire, R. Anufriev, R. Yanagisawa, A. Ramiere, S. Volz, and M. Nomura, Heat conduction tuning by wave nature of phonons, Sci. Adv. **3**, e1700027 (2017).

[13] J. Du, W. Shen, S. Su, and J. Chen, Quantum thermal management devices based on strong coupling qubits, Phys. Rev. E **99**, 062123 (2019).

[14] T. Çağın, J. B. Haskins, A. Kınacı, and C. Sevik, in *Computational Materials, Chemistry, and Biochemistry: From Bold Initiatives to the Last Mile* (Springer, 2021), p. 451.

[15] W. Feng, K. Kikuchi, M. Hidaka, H. Yamamori, Y. Araga, K. Makise, and S. Kawabata, Thermal management of a 3D packaging structure for superconducting quantum annealing machines, Appl. Phys. Lett. **118**, 174004 (2021).

[16] G. Chen, Non-Fourier phonon heat conduction at the microscale and nanoscale, Nat. Rev. Phys. **3**, 555 (2021).

[17] H. Casimir, Note on the conduction of heat in crystals, Physica **5**, 495 (1938).

[18] M. Knudsen, *The Kinetic Theory of Gases* (Methuen and Co. and John Wiley and Sons Inc., New York, 1950).

[19] A. Cepellotti, G. Fugallo, L. Paulatto, M. Lazzeri, F. Mauri, and N. Marzari, Phonon hydrodynamics in two-dimensional materials, Nat. Commun. **6**, 1 (2015).

[20] M. Quintanilla and L. M. Liz-Marzan, Guiding rules for selecting a nanothermometer, Nano Today **19**, 126 (2018).

[21] F. Reverter, A tutorial on thermal sensors in the 200th anniversary of the Seebeck effect, IEEE Sens. J. **21**, 22122 (2021).

[22] J. Qiao and D. Zhang, Extension of on-chip thermometry of metal strips toward sub-10 k regime, Appl. Phys. Lett. **120**, 173507 (2022).

[23] X. Liu, S. Akerboom, M. D. Jong, I. Mutikainen, S. Tanase, A. Meijerink, and E. Bouwman, Mixed-lanthanoid metal-organic framework for ratiometric cryogenic temperature sensing, Inorg. Chem. **54**, 11323 (2015).

[24] C. Bradac, S. F. Lim, H.-C. Chang, and I. Aharonovich, Optical nanoscale thermometry: From fundamental mechanisms to emerging practical applications, Adv. Opt. Mater. **8**, 2000183 (2020).

[25] Y. Chen, T. N. Tran, N. M. H. Duong, C. Li, M. Toth, C. Bradac, I. Aharonovich, A. Solntsev, and T. T. Tran, Optical thermometry with quantum emitters in hexagonal boron nitride, ACS Appl. Mater. Interfaces **12**, 25464 (2020).

[26] J. Zhang, H. He, T. Zhang, L. Wang, M. Gupta, J. Jing, Z. Wang, Q. Wang, K. H. Li, and K. K.-Y. Wong, *et al.*, Two-photon excitation of silicon-vacancy centers in nanodiamonds for all-optical thermometry with a noise floor of 6.6 mk $Hz^{-1/2}$, J. Phys. Chem. C **127**, 3013 (2023).

[27] J. S. Reparaz, E. Chavez-Angel, M. R. Wagner, B. Graczykowski, J. Gomis-Bresco, F. Alzina, and C. M. Sotomayor Torres, A novel contactless technique for thermal field mapping and thermal conductivity determination: Two-laser Raman thermometry, Rev. Sci. Instrum. **85**, 034901 (2014).

[28] E. Chávez-Ángel, J. S. Reparaz, J. Gomis-Bresco, M. R. Wagner, J. Cuffe, B. Graczykowski, A. Shchepetov, H. Jiang, M. Prunnila, and J. Ahopelto, *et al.*, Reduction of the thermal conductivity in free-standing silicon nanomembranes investigated by non-invasive Raman thermometry, APL Mater. **2**, 012113 (2014).

[29] S. Sandell, E. Chávez-Ángel, A. El Sachat, J. He, C. M. Sotomayor Torres, and J. Maire, Thermoreflectance techniques and Raman thermometry for thermal property characterization of nanostructures, J. Appl. Phys. **128**, 131101 (2020).

[30] N. Zen, T. A. Puurtinen, T. J. Isotalo, S. Chaudhuri, and I. J. Maasilta, Engineering thermal conductance using a two-dimensional phononic crystal, Nat. Commun. **5**, 1 (2014).

[31] W. Jang, Z. Chen, W. Bao, C. N. Lau, and C. Dames, Thickness-dependent thermal conductivity of encased graphene and ultrathin graphite, Nano Lett. **10**, 3909 (2010).

[32] T. Chihara, M. Umezawa, K. Miyata, S. Sekiyama, N. Hosokawa, K. Okubo, M. Kamimura, and K. Soga, Biological deep temperature imaging with fluorescence lifetime of rare-earth-doped ceramics particles in the second NIR biological window, Sci. Rep. **9**, 1 (2019).

[33] M. D. Dramićanin, Trends in luminescence thermometry, J. Appl. Phys. **128**, 040902 (2020).

[34] J. Anaya, S. Rossi, M. Alomari, E. Kohn, L. Tóth, B. Pécz, and M. Kuball, Thermal conductivity of ultrathin nano-crystalline diamond films determined by Raman thermography assisted by silicon nanowires, Appl. Phys. Lett. **106**, 223101 (2015).

[35] M. T. Mitchison, T. Fogarty, G. Guarnieri, S. Campbell, T. Busch, and J. Goold, *In Situ* Thermometry of a Cold Fermi Gas via Dephasing Impurities, Phys. Rev. Lett. **125**, 080402 (2020).

[36] S. Razavian, C. Benedetti, M. Bina, Y. Akbari-Kourbolagh, and M. G. Paris, Quantum thermometry by single-qubit dephasing, Eur. Phys. J. Plus **134**, 284 (2019).

[37] D. Xie, C. Xu, and A. M. Wang, Optimal quantum thermometry by dephasing, Quantum Inf. Process. **16**, 1 (2017).

[38] C. Toninelli, I. Gerhardt, A. Clark, A. Reserbat-Plantey, S. Götzinger, Z. Ristanović, M. Colautti, P. Lombardi, K. Major, and I. Deperasińska, *et al.*, Single organic molecules for photonic quantum technologies, Nat. Mater. **20**, 1615 (2021).

[39] S. Pazzagli, P. Lombardi, D. Martella, M. Colautti, B. Tiribilli, F. S. Cataliotti, and C. Toninelli, Self-assembled nanocrystals of polycyclic aromatic hydrocarbons show photostable single-photon emission, ACS Nano **12**, 4295 (2018).

[40] A. A. Nicolet, P. Bordat, C. Hofmann, M. A. Kol'chenko, B. Kozankiewicz, R. Brown, and M. Orrit, Single dibenzoterrylene molecules in an anthracene crystal: Main insertion sites, ChemPhysChem **8**, 1929 (2007).

[41] R. M. Hochstrasser and P. N. Prasad, Phonon sidebands of electronic transitions in molecular crystals and mixed crystals, J. Chem. Phys. **56**, 2814 (1972).

[42] A. Norambuena, S. A. Reyes, J. Mejía-Lopéz, A. Gali, and J. R. Maze, Microscopic modeling of the effect of phonons on the optical properties of solid-state emitters, Phys. Rev. B **94**, 134305 (2016).

[43] M. Reitz, C. Sommer, B. Gurlek, V. Sandoghdar, D. Martin-Cano, and C. Genes, Molecule-photon interactions in phononic environments, Phys. Rev. Res. **2**, 033270 (2020).

[44] C. Clear, R. C. Schofield, K. D. Major, J. Iles-Smith, A. S. Clark, and D. P. McCutcheon, Phonon-Induced Optical Dephasing in Single Organic Molecules, Phys. Rev. Lett. **124**, 153602 (2020).

[45] W. Chen, P. Roelli, H. Hu, S. Verlekar, S. P. Amirtharaj, A. I. Barreda, T. J. Kippenberg, M. Kovylina, E. Verhagen, and A. Martínez, *et al.*, Continuous-wave frequency upconversion with a molecular optomechanical nanocavity, Science **374**, 1264 (2021).

[46] B. Gurlek, V. Sandoghdar, and D. Martin-Cano, Engineering Long-Lived Vibrational States for an Organic Molecule, Phys. Rev. Lett. **127**, 123603 (2021).

[47] R. Duquennoy, M. Colautti, R. Emadi, P. Majumder, P. Lombardi, and C. Toninelli, Real-time two-photon interference from distinct molecules on the same chip, Optica **9**, 731 (2022).

[48] S. Checcucci, P. Lombardi, S. Rizvi, F. Sgrignuoli, N. Gruhler, F. B. Dieleman, F. S. Cataliotti, W. H. Pernice, M. Agio, and C. Toninelli, Beaming light from a quantum

emitter with a planar optical antenna, Light: Sci. Appl. **6**, e16245 (2017).

[49] M. D. Dramićanin, Sensing temperature via downshifting emissions of lanthanide-doped metal oxides and salts. A review, Methods Appl. Fluoresc. **4**, 042001 (2016).

[50] H. Zhou, M. Sharma, O. Berezin, D. Zuckerman, and M. Y. Berezin, Nanothermometry: From microscopy to thermal treatments, ChemPhysChem **17**, 27 (2016).

[51] Y. Chen, S. White, E. A. Ekimov, C. Bradac, M. Toth, I. Aharonovich, and T. T. Tran, Ultralow-power cryogenic thermometry based on optical-transition broadening of a two-level system in diamond, ArXiv:2211.02205 (2022).

[52] R. Martínez-Sala, J. Sancho, J. V. Sánchez, V. Gómez, J. Llinares, and F. Meseguer, Sound attenuation by sculpture, Nature **378**, 241 (1995).

[53] T. Gorishnyy, C. K. Ullal, M. Maldovan, G. Fytas, and E. Thomas, Hypersonic Phononic Crystals, Phys. Rev. Lett. **94**, 115501 (2005).

[54] O. Florez, G. Arregui, M. Albrechtsen, R. Ng, J. Gomis-Bresco, S. Stobbe, C. Sotomayor-Torres, and P. D. García, Engineering nanoscale hypersonic phonon transport, Nat. Nanotechnol. **17**, 947 (2022).

[55] N. W. Ashcroft and N. D. Mermin, *Solid State Physics* (Cengage Learning, 2022).

[56] C. Schinke, P. Christian Peest, J. Schmidt, R. Brendel, K. Bothe, M. R. Vogt, I. Kröger, S. Winter, A. Schirmacher, and S. Lim, *et al.*, Uncertainty analysis for the coefficient of band-to-band absorption of crystalline silicon, AIP Adv. **5**, 067168 (2015).

[57] M. Nomura, R. Anufriev, Z. Zhang, J. Maire, Y. Guo, R. Yanagisawa, and S. Volz, Review of thermal transport in phononic crystals, Mater. Today Phys. **22**, 100613 (2022).

[58] J. Maire, Ph.D. thesis, Ecole Doctorale d'Electronique, Electrotechnique et Automatique, Ecole Centrale de Lyon, 2015.

[59] R. Anufriev, J. Maire, and M. Nomura, Reduction of thermal conductivity by surface scattering of phonons in periodic silicon nanostructures, Phys. Rev. B **93**, 045411 (2016).

[60] R. Anufriev, A. Ramiere, J. Maire, and M. Nomura, Heat guiding and focusing using ballistic phonon transport in phononic nanostructures, Nat. Commun. **8**, 1 (2017).

[61] M. Nomura, J. Nakagawa, Y. Kage, J. Maire, D. Moser, and O. Paul, Thermal phonon transport in silicon nanowires and two-dimensional phononic crystal nanostructures, Appl. Phys. Lett. **106**, 143102 (2015).

[62] C. J. Glassbrenner and G. A. Slack, Thermal conductivity of silicon and germanium from 3 k to the melting point, Phys. Rev. **134**, A1058 (1964).

[63] R. Anufriev, J. Ordonez-Miranda, and M. Nomura, Measurement of the phonon mean free path spectrum in silicon membranes at different temperatures using arrays of nanoslits, Phys. Rev. B **101**, 115301 (2020).